Chemical Science

EDGE ARTICLE

View Article Online
View Journal | View Issue

Cite this: *Chem. Sci.*, 2019, **10**, 614

All publication charges for this article have been paid for by the Royal Society of Chemistry

Topological self-template directed synthesis of multi-shelled intermetallic Ni_3Ga hollow microspheres for the selective hydrogenation of alkyne†

Mingzhen Hu,[ab] Wenjuan Yang,[ac] Shoujie Liu,[ad] Wei Zhu,[a] Yang Li,[a] Botao Hu,[a] Zheng Chen,[a] Rongan Shen,[a] Weng-Chon Cheong,[a] Yu Wang,[a] Kebin Zhou, *[b] Qing Peng,[a] Chen Chen *[a] and Yadong Li [a]

Received 18th July 2018
Accepted 18th October 2018

DOI: 10.1039/c8sc03178a

rsc.li/chemical-science

Multi-shelled hollow structured materials featuring large void volumes and high specific surface areas are very promising for a variety of applications. However, controllable synthesis of multi-shelled hollow structured intermetallic compounds remains a formidable challenge due to the high annealing temperature commonly required for the formation of intermetallic phases. Here, a topological self-template strategy was developed to solve this problem. Using this strategy, we prepared well-defined multi-shelled intermetallic Ni_3Ga hollow microspheres (Ni_3Ga-MIHMs) as disclosed by the HAADF-STEM, HRTEM, and EDS characterizations, and the BET specific surface areas of them measured as much as 153.4 $m^2\ g^{-1}$. XRD and EXAFS spectral characterizations revealed the atomically ordered intermetallic phase nature of the Ni_3Ga-MIHMs. The selective hydrogenation of acetylene catalytic evaluation results further demonstrated excellent catalytic properties of the Ni_3Ga-MIHMs, which results from the more energetically facile reaction pathway for acetylene hydrogenation and ethylene desorption over it as revealed by DFT calculations. Besides, this strategy is also extendable to synthesize other multi-shelled intermetallic Ni_3Sn_4 hollow microspheres, and is expected to open up new opportunities for rational design and preparation of novel structured and highly efficient intermetallics.

Introduction

Atomically ordered intermetallic compounds have gained great research interest in a variety of fields such as heterogeneous catalysis,[1–6] energy conversion,[7–10] and environmental engineering,[11] by virtue of their intriguing electronic and structural properties. However, the formation of intermetallic phases commonly demands a high annealing temperature, making it a formidable challenge to fabricate intermetallic materials in a manipulatable manner.[12,13] For example, a conventional high-temperature melting route can only make bulk intermetallic compounds.[14] Wet chemistry methods provide more opportunities to prepare nano-sized intermetallics by employing capping ligand-assisted protocols, but unavoidable particle aggregation during the high-temperature annealing treatment or removal of capping ligands process generally occurs.[15,16] As a consequence, it remains a major challenge to synthesize well-defined intermetallic compounds with novel morphologies such as multi-shelled hollow structures featuring large void volumes and high specific surface areas.[17–19] Actually, multi-shelled hollow structured materials have been widely employed in many promising fields due to their more abundant surface-exposed active sites and more facile mass transfer pathways.[20–23] Great research efforts have been directed to the fabrication of multi-shelled hollow structured metal oxides, metal sulfides, and metal phosphides, *etc.*[24] However, it is quite surprising that little attention is given to the preparation of multi-shelled intermetallics, which may arise from the great difficulty in keeping the multi-shelled hollow structures under high annealing temperatures. Herein, we propose a topological self-template strategy that involves a simultaneous annealing-reduction process of an initial densely stacked template to create well-defined multi-shelled intermetallics. Using this method, we successfully fabricated multi-shelled intermetallic Ni_3Ga hollow microspheres (Ni_3Ga-MIHMs) featuring large void volumes and high specific surface areas (as much as 153.4 m^2

[a]*Department of Chemistry, Tsinghua University, Beijing 100084, P. R. China. E-mail: cchen@mail.tsinghua.edu.cn*

[b]*School of Chemical Sciences, University of Chinese Academy of Sciences, Beijing 100049, P. R. China. E-mail: kbzhou@ucas.ac.cn*

[c]*School of Chemistry and Chemical Engineering, Yulin University, Yulin City 719000, Shaanxi, P. R. China*

[d]*College of Chemistry and Materials Science, Anhui Normal University, Wuhu 241000, P. R. China*

† Electronic supplementary information (ESI) available: Experimental and DFT calculation information. See DOI: 10.1039/c8sc03178a

g^{-1}). The prepared Ni_3Ga-MIHMs exhibit excellent catalytic properties toward selective hydrogenation of acetylene, an industrially important process,[25,26] benefiting from their novel structures and energetically more favorable pathway for acetylene hydrogenation and ethylene desorption over it as revealed by DFT calculations. Besides, this strategy is also extendable to prepare other multi-shelled intermetallic Ni_3Sn_4 hollow microspheres, showing excellent generality of this approach.

Results and discussion

Synthesis and characterization of Ni_3Ga-MIHMs

The schematic preparation process of Ni_3Ga-MIHMs is displayed in Fig. 1a. By a facile topological self-template strategy, well-structured multi-shelled intermetallic Ni_3Ga hollow microspheres were successfully prepared. Fig. S1† shows that after a hydrothermal process, composite solid spheres composed of evenly dispersed metal elements (Ni and Ga), carbon, and oxygen are first obtained. XRD analysis in Fig. S2† further reveals the amorphous nature of these composite solid spheres. To explore the appropriate calcination temperature, these composite solid spheres were then subjected to thermogravimetric analysis. Based on the TGA results in Fig. S3,† their calcination temperature was determined as 600 °C. Fig. S4† is the TEM image of the composite solid spheres after 600 °C calcination treatment in air. It was found that after calcination the morphology of these spheres was readily transformed from solid to hollow, consisting of densely stacked nanoparticles. Corresponding XRD analysis in Fig. S5† further indicates that these amorphous composite solid spheres have also been turned into a mixed-phase of NiO (JCPDS 47-1049) and Ga_2O_3 (JCPDS 20-0426) after 600 °C calcination. Taking advantage of a further reduction treatment, the above mixed-phase hollow spheres become more loosely piled, generating well-defined multi-shelled hollow microspheres as displayed by the TEM images in Fig. 1b and c and SEM images in Fig. S6.† The high-resolution TEM (HRTEM) image in the inset of Fig. 1c shows that the lattice fringe of 0.21 nm is well assigned to that of the (111) plane of cubic intermetallic Ni_3Ga (JCPDS 65-0141), showing the atomically ordered intermetallic phase nature of these multi-shelled hollow microspheres, which is well in accord with the following XRD and EXAFS characterizations. The well-defined multi-shelled hollow structures of these Ni_3Ga-MIHMs are further confirmed by the corresponding EDS elemental mapping characterizations as displayed in Fig. 1d. The homogeneously distributed Ni and Ga elements show the well-defined ensemble structures of Ni_3Ga-MIHMs. Additionally, the Ni/Ga atom ratio of these Ni_3Ga-MIHMs is measured as 2.96 : 1 by ICP-OES, which is in excellent agreement with the

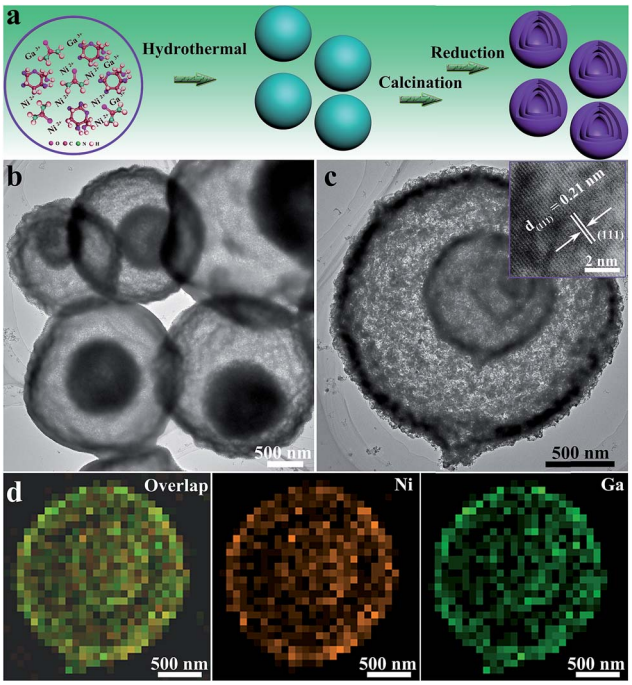

Fig. 1 (a) Schematic preparation process of the multi-shelled intermetallic Ni_3Ga hollow microspheres (Ni_3Ga-MIHMs) using a topological self-template strategy. (b) Overall TEM images of the prepared Ni_3Ga-MIHMs. (c) TEM image of a single multi-shelled intermetallic Ni_3Ga hollow microsphere (Ni_3Ga-MIHM). The inset of (c) is a corresponding HRTEM image of the Ni_3Ga-MIHMs. (d) EDS elementary mapping images of the Ni_3Ga-MIHM.

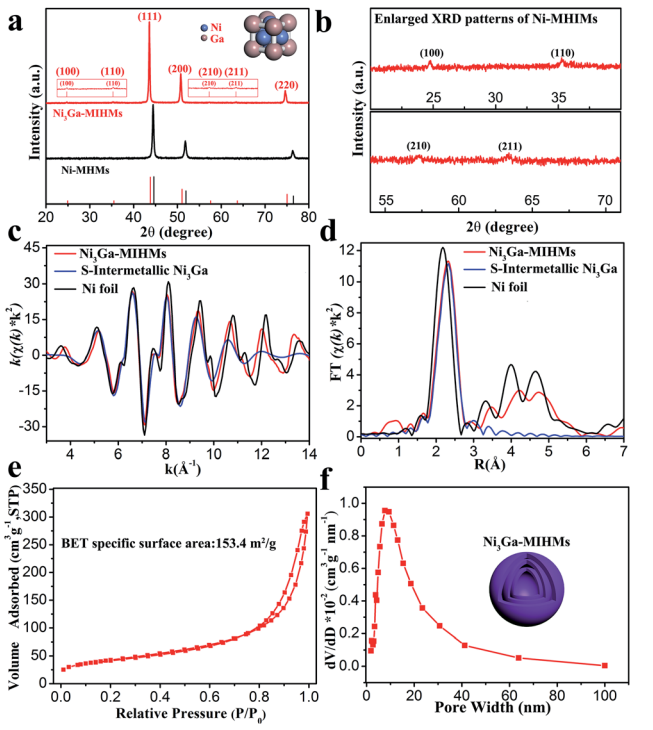

Fig. 2 (a) XRD patterns of the prepared Ni_3Ga-MIHMs and Ni-MHMs. The red vertical lines represent the standard peaks of Ni_3Ga (JCPDS 65-0141) and the black vertical lines represent the standard peaks of Ni (JCPDS 04-0850). (b) Enlarged XRD patterns of the Ni_3Ga-MIHMs. Fourier transforms of the Ni K-edge EXAFS oscillations in the (c) *k* space and in the (d) *R* space of the prepared Ni_3Ga-MIHMs and Ni foil. S-Intermetallic Ni_3Ga represents the simulated standard Ni_3Ga oscillation mode. (e) Nitrogen adsorption–desorption isotherm and (f) corresponding pore size distribution of the prepared Ni_3Ga-MIHMs.

stoichiometric composition of Ni_3Ga. XRD analysis in Fig. 2a and b reveal the intermetallic phase nature of these multi-shelled Ni_3Ga hollow microspheres and the diffraction peaks observed at 2θ values of 24.7°, 35.3°, 43.6°, 50.8°, 57.4°, 63.5°, and 74.8° are well indexed to the (100), (110), (111), (200), (210), (211), and (220) planes of the cubic intermetallic Ni_3Ga (JCPDS 65-0141), agreeing well with the above HRTEM analysis in Fig. 1. The intermetallic phase nature of the obtained Ni_3Ga-MIHMs was further confirmed by EXAFS characterizations. As displayed in Fig. 2c, the Fourier transforms of the Ni K-edge EXAFS oscillations of the Ni_3Ga-MIHMs in the *k* space are in excellent agreement with the simulated standard peaks of intermetallic Ni_3Ga, as is also observed in the *R* space shown in Fig. 2d. Data fitting results of the EXAFS spectra are shown in Table S1.† It was found that the first shell neighbour of Ni was Ga coordination with a Ni–Ga bond length of about 2.5 Å. The second shell neighbour of Ni was Ni coordination and the Ni–Ni bond length of it was about 2.6 Å. The coordination numbers of Ni–Ga and Ni–Ni were calculated to be 7.9 and 4.0, respectively. These results are well in accord with previous reports for intermetallic Ni_3Ga, which undoubtedly reveals the intermetallic Ni_3Ga phase nature of the above prepared Ni_3Ga-MIHMs.[27] XPS analysis was further employed to characterize the surface structures of the prepared Ni_3Ga-MIHMs. Fig. S7a† is the Ga 2p XPS spectra of the prepared Ni_3Ga-MIHMs. It was found that binding energy positions of the Ni_3Ga-MIHMs centered at 1116.6 eV and 1118.3 eV were well assigned to the Ga $2p_{3/2}$ peaks of Ga^0 and Ga^+, respectively.[28] Ni 2p XPS spectra of the prepared Ni_3Ga-MIHMs in Fig. S7b† further demonstrates that binding energy positions centered at 852.2 eV and 855.2 eV are well in line with the Ni $2p_{3/2}$ peaks of Ni^0 and Ni^{2+}.[5,29,30] The binding energy values of the Ga 2p XPS peaks and Ni 2p XPS peaks of Ni_3Ga-MIHMs are in excellent agreement with a previous report of intermetallic Ni_3Ga.[5] In the current case, the emerged high valence oxidation species in Ni_3Ga-MIHMs are most likely due to surface oxidation when exposed to ambient atmosphere as has been frequently revealed by reported findings.[31,32] The Brunauer–Emmett–Teller (BET) specific surface area and pore volume of these multi-shelled Ni_3Ga hollow microspheres were measured by nitrogen adsorption–desorption characterizations to be as much as 153.4 $m^2\ g^{-1}$ and 0.461 $cm^3\ g^{-1}$ with an average pore size of 14 nm as displayed in Fig. 2e and f, which is derived from the multi-shelled hollow sphere structures with large void volume.

Selective hydrogenation of alkyne evaluation over Ni_3Ga-MIHMs

The well-defined Ni_3Ga intermetallic phase nature, multi-shelled hollow sphere structures and large specific surface areas impart these Ni_3Ga-MIHMs with great potentials for selective hydrogenation of acetylene, an industrially significant reaction.[33–38] As shown in Fig. 3a and b, commercial Pd/C catalysts demonstrate full conversion of acetylene in the testing temperatures ranging from 100 °C to 130 °C, but the corresponding ethylene selectivity is quite poor and below 20%. Strikingly, the prepared Ni_3Ga-MIHMs exhibit excellent

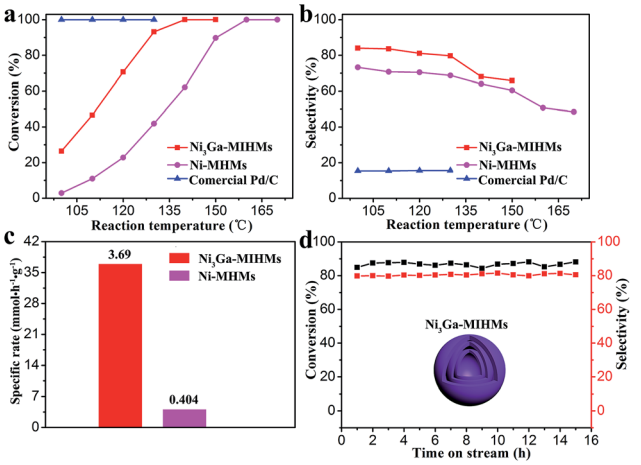

Fig. 3 (a) Acetylene conversion and (b) ethylene selectivity as a function of temperature over the Ni_3Ga-MIHMs, Ni-MHMs, and commercial Pd/C catalysts. (c) The specific rate of the prepared Ni_3Ga-MIHMs and Ni-MHMs at 100 °C. (d) Stability test over the Ni_3Ga-MIHMs as a function of time at 125 °C.

catalytic selectivity toward ethylene (around 80%) in a wide range of reaction temperatures (100–130 °C). Only when acetylene content was near to total conversion, did the corresponding ethylene selectivity demonstrate a slight decrease. This was a common phenomenon in the acetylene hydrogenation reaction and could be ascribed to the different adsorption strengths of acetylene and ethylene as has already well been disclosed by previous reports.[39] Acetylene is more thermodynamically favorable to realize adsorption and activation than ethylene. However, when acetylene was near to full conversion, ethylene could competitively adsorb on the active sites, which led to the decrease of ethylene selectivity. Moreover, the full conversion of acetylene over Ni_3Ga-MIHMs was obtained as low as 140 °C.

The multi-shelled Ni hollow microspheres (Ni-MHMs) are also fabricated as a contrast catalyst as shown in Fig. 2 and S8.† It was found that the fabricated Ni-MHMs demonstrated poor catalytic activity toward acetylene hydrogenation and the total conversion temperature of acetylene reached as high as 160 °C, showing an obvious increase in comparison with that of the Ni_3Ga-MIHMs. Besides, corresponding ethylene selectivity over the Ni-MHMs also shows an evident decrease as compared with the Ni_3Ga-MIHMs displayed in Fig. 3b. Fig. 3c is the specific rate of the Ni_3Ga-MIHMs and Ni-MHMs. It shows that the specific rate of the Ni_3Ga-MIHMs (3.69 mmol $h^{-1}\ g^{-1}$) is more than 9-fold than that of the Ni-MHMs (0.404 mmol $h^{-1}\ g^{-1}$).

DFT analysis of corresponding reaction mechanism over Ni_3Ga-MIHMs

To better understand the underlying reason of the astonishing catalytic properties difference between the Ni_3Ga-MIHMs and Ni-MHMs, DFT calculations were employed as shown in Fig. 4, 5, and S8–S12.† We investigated the whole catalytic process from the following three aspects: adsorption of acetylene hydrogenation species, transition states of acetylene hydrogenation, and selectivity of acetylene hydrogenation to ethylene.

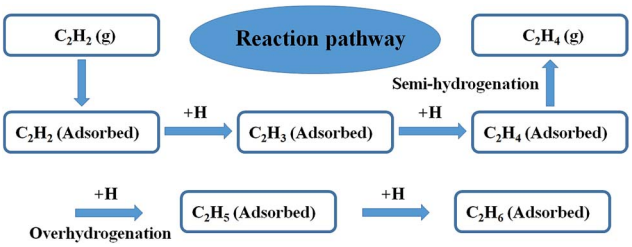

Fig. 4 The reaction pathways of selective hydrogenation of alkyne.

To make a more generalized model system, we further employed a model unit cell of 1 : 1 intermetallic cubic with a space group of *Pm3m* as a model system to simulate the intermetallic Ni_3Ga structures. Periodic slab models of Ni_3Ga (111) and Ni (111) were used to simulate hydrogenation reactivity of Ni_3Ga and Ni based on thermodynamics. To further demonstrate the reaction pathway of selective hydrogenation of alkyne over the built model Ni_3Ga (111) and Ni (111) systems, we have also drawn a reaction pathway map as displayed in Fig. 4. Initially, acetylene (C_2H_2) gas would adsorb on the surface of the catalyst. Then, the adsorbed C_2H_2 was successively hydrogenated to generate C_2H_3(ad) and C_2H_4(ad). In the following step, the generated C_2H_4(ad) was further over hydrogenated to produce C_2H_5(ad) or selectively semi-hydrogenated to form target product (C_2H_4 gas). This step is of great importance in determining corresponding C_2H_4 selectivity.

Adsorption of acetylene hydrogenation species

The adsorption structures and corresponding energies of C_2H_2 and C_2H_4 were calculated and are shown in Fig. S9–S13 and Tables S1 and S2.† The adsorption energies of C_2H_2 on the Ni_3Ga (111) and Ni (111) are −1.80 and −2.83 eV with a C–H bond length of 1.94 Å and 1.89 Å, respectively, showing effective reactivity of Ni sites of the model Ni_3Ga (111) and Ni (111). Moreover, the adsorption energy of C_2H_4 on Ni_3Ga (111) and Ni (111) are −0.94 and −0.75 eV, with C–H bond lengths of 2.15 Å and 2.03 Å, respectively, which implies that C_2H_4 can be further hydrogenated to C_2H_6. On the Ni (111) surface, C_2H_2 tends to bind to Ni atoms with a multi-σ bonding mode and a μ-bridge configuration.[5,40] On the Ni_3Ga (111) surface, all the adsorbents are bonded to Ni atoms with a similar adsorption mode as on the Ni (111) surface rather than Ga atoms because Ga is not the prime active component.[5] Besides the adsorption and activation of C_2H_2 molecules, H_2 adsorption and activation are also of great importance in determining corresponding reactivity. According to the Horiuti–Polanyi mechanism,[41] H_2 adsorption energies on Ni_3Ga (111) and Ni (111) are calculated as 0.127 eV and −0.285 eV, respectively, as shown in Fig. S13.† To be noted, H_2 dissociation over the Ni_3Ga (111) is almost barrierless with a barrier energy of only 0.0086 eV, but H_2 molecule dissociation is more challenging upon the Ni (111) with the barrier energy increased over 4-fold than that over the Ni_3Ga (111). Besides, the H_2 dissociation exothermic energy value of Ni_3Ga (111) (1.51 eV) is also much larger than that of Ni (111) (0.98 eV), further revealing the Ni_3Ga (111) is more reactive for hydrogen disassociation and activation, which is of great significance to corresponding reaction activity.

Transition states of acetylene hydrogenation

Energy profiles (energy *vs.* reaction coordinates) of the whole acetylene hydrogenation pathways are depicted in Fig. 5. The alkyne hydrogenation barriers over the Ni (111) are 0.92 eV (TS1), 0.68 eV (TS2), and 0.39 eV (TS3), respectively. The rate-determining step is the first hydrogenation step (from C_2H_2 to C_2H_3) because the barriers of this step are the largest among the TS1, TS2, and TS3. By comparison, the hydrogenation barriers of alkyne over the Ni_3Ga (111) are 1.08 eV (TS1), 0.61 eV (TS2), and 1.22 eV (TS3) with an exothermic energy of 0.61 eV, 0.25 eV, and 0.04 eV, respectively as demonstrated in Table S2.† The rate-determining step of it is the third step owing to largest barrier energy, which is different from the Ni (111) reaction pathway in which the first hydrogenation step is the rate-determining step. This result also implies that C_2H_4 is more difficult to hydrogenate to C_2H_5(ad) over the Ni_3Ga (111), which is very favorable to realize high C_2H_4 selectivity.

Selectivity of acetylene hydrogenation to ethylene

Since the adsorbed ethylene still has an unsaturated C=C bond, it can be over hydrogenated to form ethane, which decreases corresponding ethylene selectivity. To avoid this effect, we should first reveal the underlying reason that determines ethylene selectivity and develop more effective measures to improve ethylene selectivity. As indicated in Fig. 5, the ethylene gas desorption energy value upon the Ni_3Ga (111) is 0.94 eV, which is much lower than that of the corresponding ethylene hydrogenation barrier (TS3, 1.22 eV), disclosing that ethylene is more prone to desorb in the form of gas rather than to be hydrogenated to ethane. However, as for the Ni (111), the ethylene desorption energy value over it is 0.75 eV, which is much higher than that of the corresponding ethylene hydrogenation barrier (TS3, 0.39 eV), which reveals that ethylene

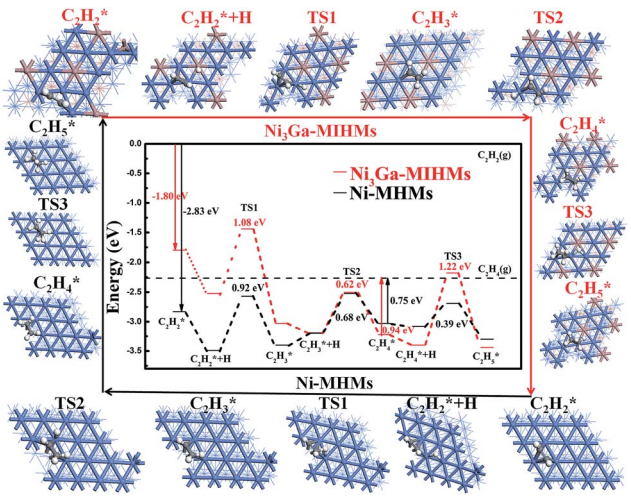

Fig. 5 Potential energy diagram by DFT calculations for the C_2H_2 hydrogenation process over the Ni_3Ga-MIHMs and Ni-MHMs.

prefers to further hydrogenate to ethane rather than desorption, leading to the low ethylene selectivity of the it. What's more, the selectivity of ethylene formation could be estimated by the difference (ΔE_a) between the hydrogenation barrier and the desorption barrier of ethylene, and a more positive ΔE_a value indicates better selectivity to ethylene.[42] The ΔE_a of Ni_3Ga (111) and Ni (111) are calculated to be 0.28 eV and −0.36 eV, respectively, illustrating that Ni_3Ga (111) is more effective in obtaining high selectivity of ethylene. The generally simulated reaction pathway nicely explains the experimental results as displayed in Fig. 3–5, and is also in good agreement with previous reports.[5,40] We believe that the DFT results are not limited to the current system and are also extendable to other systems because of the built models Ni_3Ga (111) and Ni (111).

According to DFT calculations in Table S4,† the crystal formation energy of intermetallic Ni_3Ga and Ni_3Sn_4 are −16.35 eV and −59.46 eV, respectively, which demonstrates a thermodynamically favorable path for the formation of multi-shelled intermetallic inter-metallic Ni_3Ga and Ni_3Sn_4 phases. Taking a similar approach, well-defined multi-shelled inter-metallic Ni_3Sn_4 hollow microspheres were further successfully synthesized as evidenced by the detailed XRD, HAADF-STEM, and EDS elemental mapping characterizations as demonstrated in Fig. S14–16,† showing effective generality of the topological self-template protocol. To be noted, the BET specific surface area of these multi-shelled Ni_3Sn_4 hollow microspheres amounts to 69.1 $m^2\ g^{-1}$, as shown in Fig. S16b.†

Conclusions

In summary, we have prepared well-defined multi-shelled intermetallic Ni_3Ga hollow microspheres (Ni_3Ga-MIHMs) *via* a topological self-template strategy. Detailed characterization revealed the novel structures and atomically ordered intermetallic Ni_3Ga phase nature of the fabricated Ni_3Ga-MIHMs. Selective hydrogenation of the acetylene catalytic evaluation results further showed the excellent catalytic properties of the multi-shelled intermetallic Ni_3Ga hollow microspheres, due to the more energetically favorable reaction pathway for acetylene hydrogenation and ethylene desorption over it as revealed by the corresponding DFT calculations. This strategy is also extendable to the preparation of other multi-shelled intermetallic Ni_3Sn_4 hollow microspheres, opening up new opportunities for the rational design and synthesis of novel structured and highly efficient intermetallic compound materials.

Conflicts of interest

There are no conflicts to declare.

Acknowledgements

M. Z. H., W. J. Y., and S. Z. L. contributed equally to this work. This work was supported by the National Natural Science Foundation of China (21872076, 21573119, 21866032, 21590792, 21473199, 51651201), the National Key R&D Program of China (2017YFA0700101, 2016YFA0202801) and Beijing Municipal Science & Technology Commission and Chinese Academy of Sciences. China Postdoctoral Science Foundation (2018M631486). We thank Tsinghua National Laboratory for Information Science and Technology for providing grid resources.

References

1 Q. Feng, S. Zhao, Y. Wang, J. Dong, W. Chen, D. He, D. Wang, J. Yang, Y. Zhu, H. Zhu, L. Gu, Z. Li, Y. Liu, R. Yu, J. Li and Y. Li, *J. Am. Chem. Soc.*, 2017, **139**, 7294.
2 E. W. Zhao, R. Maligal-Ganesh, C. Xiao, T.-W. Goh, Z. Qi, Y. Pei, H. E. Hagelin-Weaver, W. Huang and C. R. Bowers, *Angew. Chem.*, 2017, **129**, 3983.
3 N. Taccardi, M. Grabau, J. Debuschewitz, M. Distaso, M. Brandl, R. Hock, F. Maier, C. Papp, J. Erhard, C. Neiss, W. Peukert, A. Görling, H. P. Steinrück and P. Wasserscheid, *Nat. Chem.*, 2017, **9**, 862.
4 F. Studt, F. Abild-Pedersen, T. Bligaard, R. Z. Sørensen, C. H. Christensen and J. K. Nørskov, *Science*, 2008, **320**, 1320.
5 Y. Liu, X. Liu, Q. Feng, D. He, L. Zhang, C. Lian, R. Shen, G. Zhao, Y. Ji, D. Wang, G. Zhou and Y. Li, *Adv. Mater.*, 2016, **28**, 4747.
6 Y. Bai, H. Huang, C. Wang, R. Long and Y. Xiong, *Mater. Chem. Front.*, 2017, **1**, 1951.
7 K. Jiang, P. Wang, S. Guo, X. Zhang, X. Shen, G. Lu, D. Su and X. Huang, *Angew. Chem., Int. Ed.*, 2016, **55**, 9030.
8 Z. Qi, C. Xiao, C. Liu, T. W. Goh, L. Zhou, R. Maligal-Ganesh, Y. Pei, X. Li, L. A. Curtiss and W. Huang, *J. Am. Chem. Soc.*, 2017, **139**, 4762.
9 D. Kim, C. Xie, N. Becknell, Y. Yu, M. Karamad, K. Chan, E. J. Crumlin, J. K. Nørskov and P. Yang, *J. Am. Chem. Soc.*, 2017, **139**, 8329.
10 S. Thota, Y. Wang and J. Zhao, *Mater. Chem. Front.*, 2018, **2**, 1074.
11 M. Vandichel, A. Moscu and H. Grönbeck, *ACS Catal.*, 2017, **7**, 7431.
12 D. Wang, H. L. Xin, R. Hovden, H. Wang, Y. Yu, D. A. Muller, F. J. DiSalvo and H. D. Abruña, *Nat. Mater.*, 2012, **12**, 81.
13 G. Jiang, H. Zhu, X. Zhang, B. Shen, L. Wu, S. Zhang, G. Lu, Z. Wu and S. Sun, *ACS Nano*, 2015, **9**, 11014.
14 C. Suryanarayana, E. Ivanov and V. V. Boldyrev, *Mater. Sci. Eng., A*, 2001, **304–306**, 151.
15 D. Wang and Y. Li, *Adv. Mater.*, 2011, **23**, 1044.
16 M. Luo, Y. Sun, L. Wang and S. Guo, *Adv. Energy Mater.*, 2016, **7**, 1602073.
17 Z. Dong, X. Lai, J. E. Halpert, N. Yang, L. Yi, J. Zhai, D. Wang, Z. Tang and L. Jiang, *Adv. Mater.*, 2012, **24**, 1046.
18 Z. Dong, H. Ren, C. M. Hessel, J. Wang, R. Yu, Q. Jin, M. Yang, Z. Hu, Y. Chen, Z. Tang, H. Zhao and D. Wang, *Adv. Mater.*, 2014, **26**, 905.
19 J. Wang, N. Yang, H. Tang, Z. Dong, Q. Jin, M. Yang, D. Kisailus, H. Zhao, Z. Tang and D. Wang, *Angew. Chem.*, 2013, **125**, 6545.
20 L. Yu, X. Y. Yu and X. W. Lou, *Adv. Mater.*, 2018, 1800939, DOI: 10.1002/adma.201800939.

21 X. Zhao, R. Yu, H. Tang, D. Mao, J. Qi, B. Wang, Y. Zhang, H. Zhao, W. Hu and D. Wang, *Adv. Mater.*, 2017, **29**, 1700550.
22 D. Li, X. Zhao, R. Yu, B. Wang, H. Wang and D. Wang, *Inorg. Chem. Front.*, 2018, **5**, 535.
23 J. Qi, X. Lai, J. Wang, H. Tang, H. Ren, Y. Yang, Q. Jin, L. Zhang, R. Yu, G. Ma, Z. Su, H. Zhao and D. Wang, *Chem. Soc. Rev.*, 2015, **44**, 6749.
24 J. Wang, H. Tang, H. Wang, R. Yu and D. Wang, *Mater. Chem. Front.*, 2017, **1**, 414.
25 G. Kyriakou, M. B. Boucher, A. D. Jewell, E. A. Lewis, T. J. Lawton, A. E. Baber, H. L. Tierney, M. Flytzani-Stephanopoulos and E. C. H. Sykes, *Science*, 2012, **335**, 1209.
26 A. Borodziński and G. C. Bond, *Catal. Rev.*, 2008, **50**, 379.
27 L.-S. Hsu, Y. K. Wang, Y. L. Tai and J. F. Lee, *J. Alloys Compd.*, 2006, **413**, 11.
28 K. Schutte, A. Doddi, C. Kroll, H. Meyer, C. Wiktor, C. Gemel, G. van Tendeloo, R. A. Fischer and C. Janiak, *Nanoscale*, 2014, **6**, 5532.
29 L. S. Hsu, G. H. Gweon and J. W. Allen, *J. Phys. Chem. Solids*, 1999, **60**, 1627.
30 A. P. Tsai, S. Kameoka, K. Nozawa, M. Shimoda and Y. Ishii, *Acc. Chem. Res.*, 2017, **50**, 2879.
31 H. Zhou, X. Yang, L. Li, X. Liu, Y. Huang, X. Pan, A. Wang, J. Li and T. Zhang, *ACS Catal.*, 2016, **6**, 1054.
32 D. A. Torelli, S. A. Francis, J. C. Crompton, A. Javier, J. R. Thompson, B. S. Brunschwig, M. P. Soriaga and N. S. Lewis, *ACS Catal.*, 2016, **6**, 2100.
33 M. B. Boucher, B. Zugic, G. Cladaras, J. Kammert, M. D. Marcinkowski, T. J. Lawton, E. C. H. Sykes and M. Flytzani-Stephanopoulos, *Phys. Chem. Chem. Phys.*, 2013, **15**, 12187.
34 D. Teschner, J. Borsodi, A. Wootsch, Z. Révay, M. Hävecker, A. Knop-Gericke, S. D. Jackson and R. Schlögl, *Science*, 2008, **320**, 86.
35 H. Fei, L. Hongyang and S. Dangsheng, *Sci. China Mater.*, 2017, **60**, 1149.
36 L. Qiang, J. Shufang, L. Mufan and D. Xiangfeng, *Sci. China Mater.*, 2018, DOI: 10.1007/s40843-018-9282-1.
37 C. Wu, Y. Chen, R. Shen, W. Zhu, Y. Gong, L. Gu, Q. Peng, H. Guo and W. He, *Nano Res.*, 2018, **11**, 4883.
38 Y. Wang, Z. Chen, R. Shen, X. Cao, Y. Chen, C. Chen, D. Wang, Q. Peng and Y. Li, *Nano Res.*, 2016, **9**, 1209.
39 A. J. McCue and J. A. Anderson, *Front. Chem. Sci. Eng.*, 2015, **9**, 142.
40 D.-M. Rao, S.-T. Zhang, C.-M. Li, Y.-D. Chen, M. Pu, H. Yan and M. Wei, *Dalton Trans.*, 2018, **47**, 4198.
41 B. Yang, R. Burch, C. Hardacre, P. Hu and P. Hughes, *Catal. Sci. Technol.*, 2017, **7**, 1508.
42 B. Yang, R. Burch, C. Hardacre, G. Headdock and P. Hu, *ACS Catal.*, 2012, **2**, 1027.